BioImpacts

TUOMS PRESS

CrossMark
click for updates

Publish Free
Access

Fabrication of mesoporous silica nanoparticles for targeted delivery of sunitinib to ovarian cancer cells

Mitra Torabi[1,2], Ayuob Aghanejad[1*], Pouria Savadi[3], Abolfazl Barzegari[1], Yadollah Omidi[4], Jaleh Barar[4*]

[1]Research Center for Pharmaceutical Nanotechnology, Biomedicine Institute, Tabriz University of Medical Sciences, Tabriz, Iran
[2]Department of Pharmaceutics, Faculty of Pharmacy, Tabriz University of Medical Sciences, Tabriz, Iran
[3]Di.S.T.A.Bi.F., University of Campania "Luigi Vanvitelli", Via Vivaldi 43, 81100 Caserta, Italy
[4]Department of Pharmaceutical Sciences, College of Pharmacy, Nova Southeastern University, Fort Lauderdale, FL 33328, USA
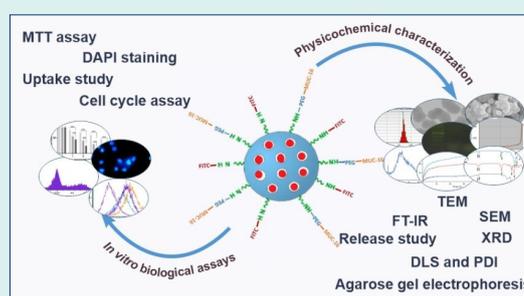
Abstract

Introduction: Mesoporous silica nanoparticles (MSNPs) are considered innovative multifunctional structures for targeted drug delivery owing to their outstanding physicochemical characteristics.

Methods: MSNPs were fabricated using the sol-gel method, and polyethylene glycol-600 (PEG_{600}) was used for MSNPs modification. Subsequently, sunitinib (SUN) was loaded into the MSNPs, MSNP-PEG and MSNP-PEG/SUN were grafted with mucin 16 (MUC16) aptamers. The nanosystems (NSs) were characterized using FT-IR, TEM, SEM, DLS, XRD, BJH, and BET. Furthermore, the biological impacts of MSNPs were evaluated on the ovarian cancer cells by MTT assay and flow cytometry analysis.

Results: The results revealed that the MSNPs have a spherical shape with an average dimension, pore size, and surface area of 56.10 nm, 2.488 nm, and 148.08 m^2g^{-1}, respectively. The cell viability results showed higher toxicity of targeted MSNPs in MUC16 overexpressing OVCAR-3 cells as compared to the SK-OV-3 cells; that was further confirmed by the cellular uptake results. The cell cycle analysis exhibited that the induction of sub-G1 phase arrest mostly occurred in MSNP-PEG/SUN-MUC16 treated OVCAR-3 cells and MSNP-PEG/SUN treated SK-OV-3 cells. DAPI staining showed apoptosis induction upon exposure to targeted MSNP in MUC16 positive OVCAR-3 cells.

Conclusion: According to our results, the engineered NSs could be considered an effective multifunctional targeted drug delivery platform for the mucin 16 overexpressing cells.

Introduction

Ovarian cancer is the eighth most prevalent form of the disease among women, although it is the fifth largest cause of death from a tumor. This disease is usually diagnosed in the metastatic phase; thus, timely diagnosis and appropriate treatment strategy offer remarkable importance.[1] It is estimated that in 2021, approximately 21 410 cases of ovarian cancer were diagnosed in the US, which caused 13 770 cases of women's death.[2] The prevalence of ovarian cancer is complicated due to the association of different heterogeneous malignancies. Early diagnosis of this disease using effective screening could be a valuable approach to improve the treatment outcomes.

Several clinical procedures such as physical examinations, computed tomography, magnetic resonance imaging, positron emission tomography, ultrasonography, and tissue biopsy in conjunction with cancer antigen 125 (CA125) detection are implemented for the diagnosis of ovarian cancer.[3] Mucin 16, also known as CA125, has been used as one of the diagnostic markers over the years. It is a glycoprotein aberrantly overexpressed in ovarian cancer cells and a key tumor marker for detecting ovarian cancer.[4,5] Although common chemotherapeutics seem to help many women, the adverse side effects are often severe, limiting their administration. One of the promising approaches to avert undesired side effects

and improve therapeutic output is targeting the cancer-specific markers overexpressed in ovarian cancer. Studies have shown that receptor tyrosine kinases (RTKs) are considered critical markers for tumor progression and resistance to chemotherapy since their complicity has been revealed in about one-third of metastatic ovarian cancer.[6] Surprisingly, recurrent drug resistant forms of ovarian cancer exhibit more sensitivity to the kinase inhibitors than platinum-based treatment regimens.[7]

Sunitinib malate, a novel multi-targeted RTK inhibitor, has demonstrated moderate effectiveness in several phase II clinical trials for ovarian cancer, showing a potential treatment regimen for the resistant recurrence of tumor in the future.[8,9] Furthermore, angiogenesis as a common phenomenon in ovarian cancer could also be efficiently inhibited by SUN. SUN is one of the foremost selective angiogenesis inhibitors targeting the vascular endothelial growth factor (VEGF); hence, it has received immense attention to combat ovarian cancer.[10-12]

Nowadays, the development of seamless drug delivery systems (DDSs) armed with imaging and targeting agents for simultaneous diagnosis and treatment of cancer has presented a greater significance because of the selectivity and specificity of their effect.[13] Pertinently, mesoporous silica nanoparticles (MSNPs) regarding their unique characteristics such as large surface area (700–1000 m^2 g^{-1}) with high drug loading efficiency, tailor-made pore size (0.6–1 cm^3 g^{-1}), outstanding biodistribution, and biocompatibility are considered as promising nanosystems (NSs) for imaging and treatment applications.[14] MSNPs depending on their capabilities can accumulate in the tumor microenvironment (TME) up to 70-fold. This preferential accumulation in tumor cells is because of two main phenomena: the increased blood vessel permeability (presence of fenestrations in vessels) and low lymphatic drainage of tissues which collectively is called the enhanced permeability and retention (EPR) effect.[15] Furthermore, the usage of biomarkers (such as ligands, antibodies, and aptamers) assembled to MSNPs, provides valuable targets to develop DDSs for active targeting.[16] The tumor-targeting efficiency of MSNPs depends on sufficient localization and penetration into tumor tissue, and then adequate binding and internalization into cancer cells.[17,18] The binding-site barrier phenomenon has been raised recently, referring to high-affinity targeting agents such as antibodies. High affinity of antibodies prevents deep penetration. They tightly bind the cells they first meet after extravasation, resulting in the inappropriate distribution in tumor tissue. Nevertheless, conjugation of aptamers to MSNPs seems to provide a robust alternative targeting tool.

The function of the aptamer is similar to the antibody with fewer limitations and immunologic responses. The aptamer is a small strand of DNA or RNA that binds to a specific target molecule. The MUC16 aptamer has been established as a biomarker for diagnostic purposes.[19]

Functionalization of MSNPs with a MUC16 targeting agent may lead to an elevation in the accumulation of the drug molecules within cancer cells via receptor-mediated endocytosis and a decrease in the off-target effects.[20]

This study was designed considering various aspects. First, the MSNPs as robust carriers were synthesized using the sol-gel method and coated with bi-carboxylic PEG$_{600}$ to improve circulation time. Then SUN, a potentially active therapeutic against recurrent ovarian cancer, was loaded in the porous structure of NPs. Then, the surface was armed with MUC16 aptamer as a homing agent, to direct the delivery system toward ovarian cancer cells. After the characterization of the engineered MSNPs, their biological impacts were evaluated on OVCAR-3 and SK-OV-3 cells.

Materials and Methods
Materials
Cetyl trimethylammonium bromide (CTAB), tetraethyl orthosilicate (TEOS), sodium hydroxide (NaOH), ethyl acetate, ammonium nitrate, dichloromethane, acetone, diethyl ether, dimethyl sulfoxide (DMSO), sodium borohydride, 3-(triethoxysilyl)propylamine were obtained from Merck (Darmstadt, Germany). Thiazolyl blue tetrazolium bromide (MTT) used in this study was purchased from Sigma Aldrich (Saint Louis, USA) and PEG$_{600}$ was obtained from Sigma Aldrich (Munich, Germany). N-hydroxy succinimide (NHS) and dicyclohexyl carbodiimide (DCC) were purchased from Alfa Aesar (Heysham, England). Human ovarian cancer OVCAR-3 and SK-OV-3 cell lines of this investigation were obtained from the National Cell Bank of Iran, Pasteur Institute (Tehran, Iran). Amino-functionalized MUC16 aptamer with the sequence of (5′-NH$_2$ (C6)ACTAGCTCCGATCTTTCTTATCTAC-3′)[21] was purchased from Bioneer (Daejeon, South Korea). All other media and cell culture components not listed were purchased from Gibco (Paisley, United Kingdom).

Preparation of MSNPs-NH2
First, the solution of CTAB (125 mg, 0.34 mmol) was prepared in 30 mL of deionized water by stirring, and the temperature was raised to 60°C. Then, NaOH (0.2 N) was added to adjust the pH of the solution to 12. Afterward, the solution of TEOS (1500 mg, 7 mmol) in ethyl acetate (1:4 V/V) was added and stirred for 3 hours at 70°C. Then the solution of 3-(triethoxysilyl) propylamine (40 mg, 0.18 mmol) in 1 mL of acetone was added to the mixture and stirred at 70°C for 3 hours to allow the formation of MSNPs. Then the nanoparticles were collected by centrifugation at 2800 ×g and washed with ethanol two times (×2). MSNPs were then re-dispersed in an ethanolic solution of ammonium nitrate (10 mg/mL) and stirred at 60°C for 3 hours. The nanoparticles were washed with ethanol (×3) and centrifuged at 2800 ×g to collect them. The MSNPs were then re-dispersed in an ethanolic solution of sodium

borohydride (5 mg/mL), stirred for 30 minutes, washed with ethanol, and collected by centrifugation at 2800 ×g.

PEG600-2NHS ester preparation

For the preparation of PEG600-2NHS, the solution of NHS (3.84 g, 33 mmol) in dichloromethane (15 mL) was combined with the solution of PEG600 (10 g, 12 mmol) in 350 mL of dichloromethane. The solution of DCC (6.88 g, 33 mmol) in dichloromethane (20 mL) was then drop-wisely added to the mixture on the stirrer. The mixture was stirred overnight at room temperature (RT), and afterward, the compounds were filtered and precipitated using diethyl ether.

PEGylation of nanoparticles (MSNP-PEG)

The solution of PEG600-2NHS (10 mg) in 1 mL of dichloromethane was added to the suspension of MSNPs (100 mg) in 4 mL of DMSO, and the stirring of the reaction mixture was performed overnight at RT. Then, nanoparticles were collected by centrifugation at 5000 ×g and washed with ethanol (×3). The final product was dried with the Labconco vacuum freeze-dryer (Kansas City, US).

Drug loading (MSNP-PEG/SUN)

To prepare for drug loading, the SUN solution in DMSO (55 mg/2 mL) was added to the suspension of MSNP-PEG in DMSO (55 mg/1 mL) and the final suspension was stirred at RT overnight. NSs were centrifuged at 5000 ×g and separated. The supernatant which contained the unloaded SUN was analyzed to determine loading efficiency. SUN-loaded MSNPs were dried using the Labconco vacuum freeze-dryer (Kansas City, US).

Determination of SUN loading efficiency

Ultraviolet /Visible (UV/Vis) spectrophotometry (Cecil CE 7500, Cambridge, UK) at λ max of 267 nm was used to evaluate SUN loading using the following equation.

$$SUN\ loading\ efficiency = 100 \times (Total\ SUN - Unloaded\ SUN)/\ Total\ SUN.$$

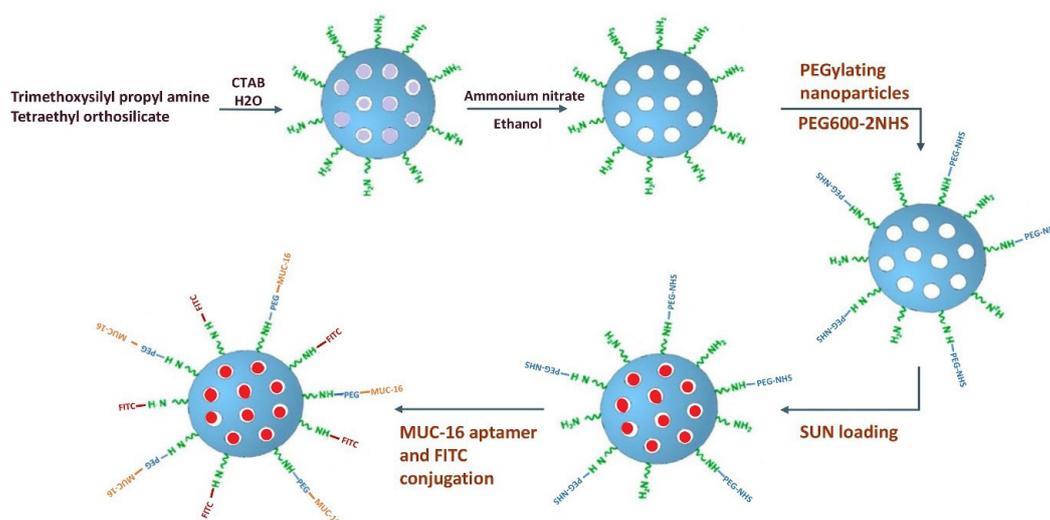### Decoration of MSNP-PEG/SUN with MUC16 aptamer

The suspension of MSNP-PEG/SUN (1.5 mg) in 600 μL nuclease-free water was added to the solution of 5′ amino-functionalized MUC16 aptamer (2.5 nmol) in 100 μL RNase-DNase water and stirred up at ambient temperature for 4 hours. The MUC16-decorated NSs were harvested by centrifugation at 2500 ×g for 15 minutes. The schematic step-by-step process of nanoparticle formation is shown in Fig. 1.

Conjugation of fluorescein isothiocyanate (FITC) to MSNP-PEG

As illustrated in Fig. 1, the MSNPs were labeled with FITC to evaluate the cellular uptake by flow cytometry. To this end, 0.5 mL of NSs suspension in DMSO (7.8 mg/mL) was combined with 0.5 mL FITC solution in DMSO (2 mg/mL) and stirred for 12 hours. Then, NSs were collected using centrifugation at 3100 ×g and washed with PBS (×3) and kept at 4°C.

Particle size, zeta potential, and surface morphology

The morphology of MSNPs was assessed by transmission electron microscopy (TEM) using LEO 906E, Carl Zeiss, Oberkochen (Germany) microscope, and scanning electron microscopy (SEM) using MIRA3 FEG-SEM (Tescan, Czechia). The size and ζ-potential of NSs were analyzed by Zetasizer, Nanotrac wave (Microtrac Inc, Montgomeryville, PA, USA). The polydispersity index (PDI) was utilized to determine the heterogeneity of nanoparticles. The functional groups and surface modifications of the NSs were confirmed using Fourier transform infrared (FT-IR) spectroscopy using Bruker

Fig. 1. Schematic representation of the MSNPs formulation. MSNPs were fabricated using the sol-gel method and modified by PEG600-2NHS. Then SUN was loaded into the MSNPs, and NSs were grafted with MUC16 aptamers.

Optik GmbH, Ettlingen (Germany) in the range of 400-4000 cm^{-1}.

Surface area analysis and pore size measurement

Specific surface area and pore size of MSNPs were calculated by Barrett-Joyner-Halenda (BJH) and Brunauer-Emmett-Teller (BET) analysis. The N$_2$ ADS/DES isotherms of samples (degassed at 120°C under vacuum for 5 hours) were evaluated at 77°K on the BELSORP MINI II apparatus (Microtrac BEL Japan). The specific surface area of the MSNPs was calculated by the BET analysis in an intermediate pressure range of P/P0= 0.01-0.45 (the linear range of the Langmuir isotherm). The BJH method evaluated the pore size distribution of MSNPs using the adsorption branch of the ADS/DES isotherms.

Agarose gel electrophoresis

The agarose gel (1% W/V) electrophoresis was carried out to verify the attachment of aptamer to the NSs. Briefly, MUC16 aptamer (2.8 nmol) was added to the MSNP-PEG (1 mg/mL) and stirred up for 4 hours. The aptamer-armed nanoparticles were collected by centrifugation at 14000 ×g for 30 minutes. Then, 10 µL of the samples (including free aptamer (2.8 nmol) and MSNP-PEG-MUC16) were mixed with 1 µL loading dye and then loaded onto the electrophoresis gel. The gel was run at 70 V for 1 hour in 1× TAE buffer and then visualized under UV illumination (Syngene IG/LHR-E, Cambridge, UK).

X-ray diffraction analysis (XRD)

The XRD analysis was conducted to determine the atomic and molecular structure of MSNPs using the Cu K radiation with 1.5406 A° as an X-ray generator. The diffraction data were recorded between 5 and 70° with the step of 0.02° on Siemens-D 5000 (Aubrey, USA).

In vitro drug release

To study the drug release from SUN-loaded nanoparticles, MSNP-PEG/SUN (2.5 mg/mL) was resuspended in 2 mL phosphate buffer release medium with pH values of 5.4, 6.4, and 7.4 as the condition of endosomes, TME, and blood, respectively and placed into a pre-swollen dialysis membrane bag (cut-off 2 kDa, Sigma Aldrich). The bag was then immersed in 198 mL of phosphate buffer and incubated at 37°C for 48 hours. The 2 mL aliquots were taken out from release media in predesignated time intervals and the volume of the solutions was retained constant by the addition of fresh media (2 mL). The concentration of released SUN from NSs was measured using UV/Vis spectrophotometry at the wavelength of 267 nm.

Cell culture

The OVCAR-3 and SK-OV-3 cells were cultured in RPMI-1640 supplemented with 10% fetal bovine serum (FBS), penicillin (100 IU/mL), and streptomycin (100 µg/mL). The cells were incubated in a humidified CO$_2$ (5%) incubator at 37°C.

In vitro cytotoxicity analysis

The prepared formulations and SUN cytotoxicity were investigated in the OVCAR-3 and SK-OV-3 cells as mucin 16 positive[22] and negative[23,24] cell lines. Both cell lines were cultivated in 96-well plates at a seeding density of 3×10^3 cells/well, and cells were allowed to stay overnight. Then, the cells were treated with varying concentrations of MSNPs based on the equivalent concentration of SUN (1, 5, 10, and 20 µM). The media was removed at the designated time intervals (24, 48 hours), and cells were exposed to 20 µL/well of MTT solution (5 mg/mL) and 180 µL of the fresh media and incubated for 4 hours at 37°C. Following the incubation period, the crystals of formazan were dissolved in DMSO (200 µL) plus Sorenson's buffer (25 µL).[25] Then, the absorbance of the product was read using an Elisa plate reader (ELX808) (BioTek Instruments, USA) at 570 nm, and the cell viability was calculated as the percentage of untreated control wells.

Flow cytometry analysis

NSs uptake evaluation

The flow cytometry analysis was carried out to evaluate the nanoparticles' uptake by OVCAR-3 and SK-OV-3 cells. Briefly, the cells were cultivated at a density of 9×10^4 cells in 6-well plates for 24 hours. Then, the samples of FITC-labeled NSs (MSNP-PEG/SUN-MUC16, MSNP-PEG/SUN, MSNP-PEG-MUC16, and MSNP-PEG) were prepared and added to the cells, allowing the internalization for 2 hours. Afterward, the cells were washed with PBS (×3), trypsinized, and centrifuged at 160 ×g for 5 minutes and analyzed using FACSCalibur® flow cytometer (Becton Dickinson, San Jose, CA, USA), with the minimum number of 1.0×10^4 cells per sample.

Cell cycle evaluation

Cell cycle analysis by quantitative content of DNA was accomplished using propidium iodide (PI) stained single-cell suspension to distinguish the cell population in different growth cycle phases.[26] Both cell lines were cultivated in 6-well plates for 24 hours and then were treated with MSNP-PEG/SUN-MUC16, MSNP-PEG/SUN, and free SUN. Subsequently, 48 hours post-seeding, the cells were washed with PBS, trypsinized, and centrifuged at 160 ×g for 5 minutes. Afterward, the cells were fixed using 70% ice-cold ethanol and incubated for 24 hours at 4°C. Next, the cells were collected by centrifugation at 200 ×g for 5 minutes and then were resuspended in 50 µL of ribonuclease enzyme solution (10 µg/mL) and 50 µL PI solution (10 µg/mL) after being washed with cold PBS. Then, the cells were incubated in a dark room for 30 minutes. Subsequently, the samples were analyzed using FACSCalibur® flow cytometer (Becton Dickinson, San Jose, CA, USA) via PI bandpass filter in

the range of 570-640 nm.

DAPI staining

DAPI staining was performed to evaluate the nuclear morphology and chromatin condensation in the treated cells. Both cell lines were cultivated with a density of 6×10^4 cells in the 12-well plates. Following one night of incubation, the cells were exposed to different formulations. Subsequently, 48 hours post-seeding, the cells were washed with PBS (×3), fixed with 4% paraformaldehyde, and permeabilized using 0.1% Triton X-100 followed by a final washing step with PBS (×3). Afterward, for staining, the cells were incubated with 200 μL/well of DAPI (200 ng/mL) in the room for 5 minutes. Finally, PBS was added to the wells to keep cells hydrated. The cells were studied under a fluorescent microscope (Cytation 5, Biotek, Winooski, USA).

Statistical analysis

The results were presented as mean ± standard deviation (SD). Statistical analysis was conducted by ANOVA using GraphPad Prism 8.0.1 software (GraphPad Software Inc., USA). A P value of less than 0.05 was determined as the statistical difference.

Results

As shown in Fig. 1, the MSNPs were synthesized using the sol-gel method. To increase biocompatibility, MSNPs were further functionalized with activated PEG_{600}-2NHS molecules. Then, MSNP-PEGs were loaded with SUN and decorated with MUC16 aptamers.

Morphological studies

As presented in Fig. 2A, the TEM micrograph of MSNP-PEG depicted a monodisperse view and porous structure of MSNPs. Moreover, according to Fig. 2B, the SEM image showed the nanoparticles' smooth surface and spherical shape.
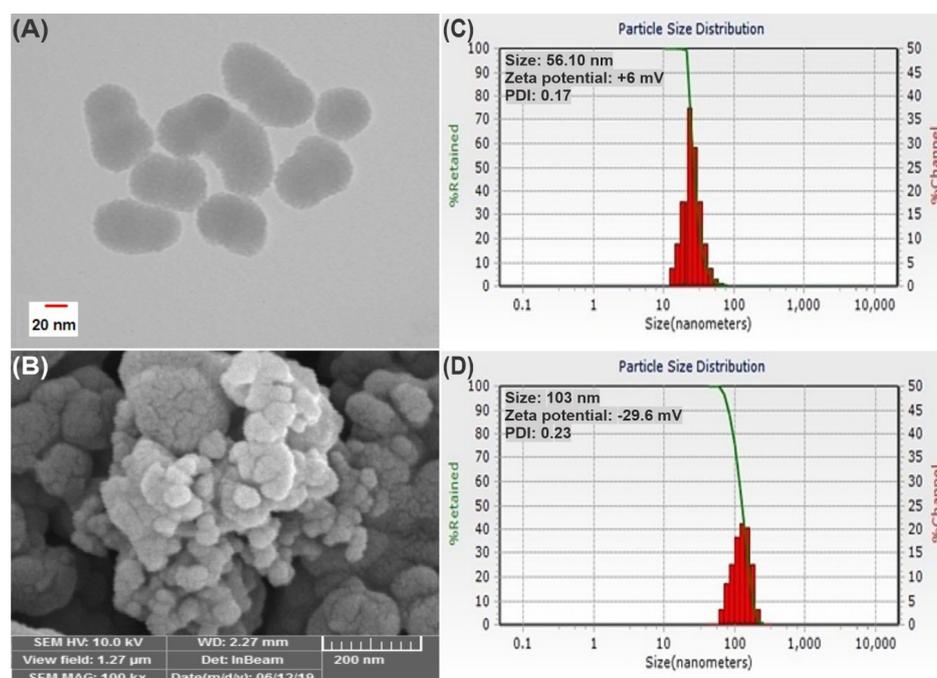
DLS and zeta potential analysis

The MSNP and MSNP-PEG had an average size of 56.10 nm and 103 nm, sequentially, and additionally, they possessed a surface charge of +6 and -29.6 mv with a PDI of 0.17 and 0.23, in the same order (Fig. 2C and 2D). This physicochemical analysis verifies that the particles were nano-sized and homogeneous. The ascent in the size of the nanoparticles also confirmed the successful PEGylation of MSNPs. It seems that the size of the nanoparticles in SEM was slightly smaller than the measured size in DLS, which may contribute to the attenuation or dehydration of MSNPs during the imaging process.

FT-IR spectroscopy

The FT-IR spectra analysis of NSs was conducted to identify the functional groups and the surface modification as illustrated in Fig. 3A. In the spectra of MSNPs, the absorption bands at 963 and 801 cm^{-1} are associated with symmetrical and asymmetrical stretching bonds of siloxane.

Moreover, the absorption band at 1095 cm^{-1} is related to the symmetrical stretching bond of Si-O. Further, the peak at 3413 cm^{-1} is attributed to the symmetrical stretching bond of the amine group of MSNPs. Moreover, the peaks at 2928 and 2859 cm^{-1} are attributed to alkane's

Fig. 2. Particle morphology analysis of MSNP-PEG with TEM and SEM imaging process, respectively (A and B). The particle size evaluation of MSNP and MSNP-PEG, sequentially (C and D). PDI: polydispersity index.

symmetrical and asymmetrical C-H stretching bonds.[26] In the spectra of PEG_{600}-2NHS, the absorption band at 1632 cm^{-1} is attributed to the symmetrical C=O stretching bond of NHS. Further, 1080 and 1206 cm^{-1} peaks are assigned to the asymmetrical C-O-C of PEG_{600} and C-N-C. The absorption peaks at 2927 and 2873 cm^{-1} are related to C-H's symmetrical and asymmetrical stretching bonds in the alkane group.[27] The spectra of MSNP-PEG and MSNP-PEG/SUN represent mostly similar absorption bands, which display that PEG-2NHS has successfully conjugated to MSNPs and the absorption band at 3004 cm^{-1} is indicative of the amine group of SUN that has been loaded into the NSs properly.[28]

Specific surface area and pore size evaluation

The ADS/DES isotherm of MSNPs demonstrated a type IV isotherm implying a mesoporous structure with a partially strong adsorption/desorption between the surface of the MSNPs and N_2 (Fig. 3B, 3C).[29] Table 1 shows the BET and BJH calculations for the surface area, pore volume, and pore size of MSNPs.

Agarose gel electrophoresis

To verify the conjugation of the MUC16 aptamer to NSs, 1% agarose gel electrophoresis was performed. As represented in Fig. 3D, MUC16 aptamer conjugated MSNP was retarded in the well compared to the MUC16 aptamer.
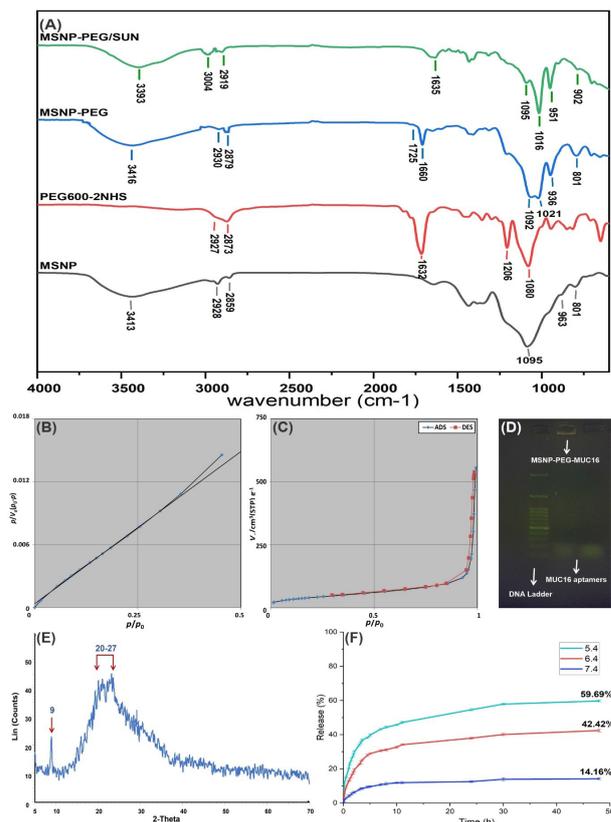
XRD analysis

As presented in Fig. 3E, the XRD results showed two sharp and broad peaks at 2θ of 9 and 20-27, which are considered the fingerprints of the MSNPs. The XRD pattern confirms the amorphous structure of the prepared MSNPs.

Determination of SUN loading efficiency and release profile

The SUN loading efficiency was 70 ± 0.69 %, calculated as the amount of SUN molecules successfully loaded into the porous structure. Drug release experiments indicated that the higher release of SUN molecules from MSNPs occurred in a pH-dependent manner and it was found that by pH reduction from 7.4 to 5.4 there was an increase in the drug release. As demonstrated in Fig. 3F, the cumulative drug release at the pH value of 7.4, 6.4, and 5.4 were $14.16 \pm 0.94\%$, $42.42 \pm 0.81\%$, and $59.69 \pm 0.91\%$, respectively after 48 hours.

Cell viability

As presented in Fig. 4, the viability of OVCAR-3 cells after 24 hours of exposure to MSNP-PEG/SUN-MUC16,
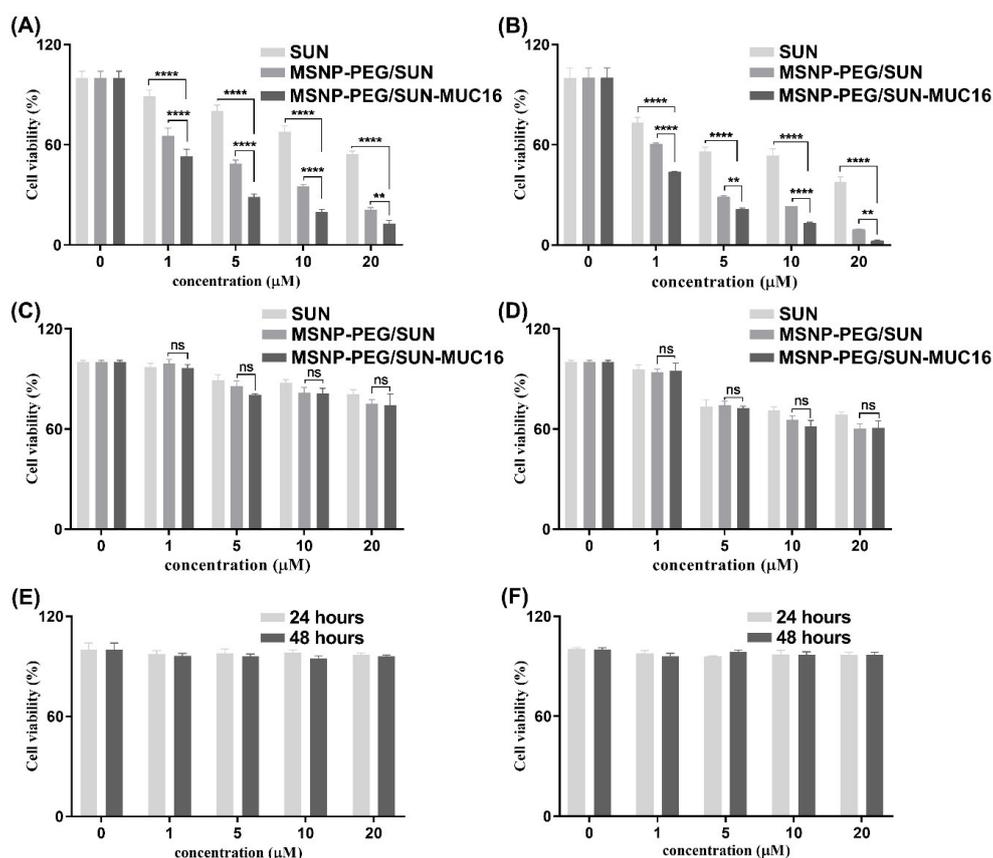

Fig. 3. FT-IR spectra of MSNP-PEG/SUN, MSNP-PEG, PEG_{600}-2NHS, and MSNP (A). The BET plot, porosity assessment, and N2 ADS/DES isotherm of MSNPs (B and C). The agarose gel electrophoresis of MUC16 aptamer conjugation to MSNP-PEG; A 50 bp DNA ladder was used in agarose gel electrophoresis (D). XRD spectrum of MSNP (E) and the release profile of SUN from MSNP-PEG/SUN based on the UV absorption in phosphate buffer with 3 different pH values after 48 hours (F). ADS: adsorption isotherm, DES: desorption isotherm.

MSNP-PEG/SUN, and SUN (at the concentration of 20 µM of SUN) was 12.81%, 21.12%, and 54.49%, respectively. Further, after 48 hours of exposure to the same treatment order, viability declined to 2.42%, 9.32%, and 37.85%. The viability of SK-OV-3 cells after 24 hours with the same order of treatments was 74.18%, 75.16%, and 80.98%. Furthermore, after 48 hours the viability declined to 60.77%, 60.26%, and 68.84%. These results showed that the cell viability in both cells was reduced in a time- and dose-dependent manner and MSNP-PEG/SUN-MUC16 could induce greater toxicity in OVCAR-3 cells than MSNP-PEG/SUN because of the MUC16 overexpression on the surface of the OVCAR-3 cell line. While the cytotoxicity of MSNP-PEG/SUN-MUC16 was similar to the toxicity of MSNP-PEG/SUN in the SK-OV-3 cell line, there was generally higher toxicity compared with SUN molecules in both cell lines. It can also be noted that there

Table 1. Surface and pore characteristics of MSNPs

Sample	BET surface area(m^2g^{-1})	Pore diameter(nm)	Pore volume(cm^3g^{-1})
MSNP	148.08	2.488	0.7955

Fig. 4. The cell viability analysis of OVCAR-3 cells (A and B) and SK-OV-3 (C and D) cells after 24 and 48 hours respectively upon treatment with SUN, MSNP-PEG/SUN-MUC16, MSNP-PEG/SUN, and SUN. The viability of OVCAR-3 (E) and SK-OV-3 (F) cells after treatment with MSNP-PEG-MUC16 for 24 and 48 hours. Data are shown as mean ± SD. The asterisks represent following level of significance; not significant (ns) $P \geq 0.05$, $*P \leq 0.05$, $**P \leq 0.01$, $***P \leq 0.001$, $****P \leq 0.0001$.

were no noticeable cytotoxic effects of MSNP-PEG and MSNP-PEG-MUC16 in both cell lines.

Cellular uptake study

The uptake flow cytometry assay was carried out to determine the cellular internalization of functionalized MMSNPs. As shown in Fig. 5, cells were exposed to the treatments in an equal concentration of 20 μM SUN for 2 hours. As expected, there was a greater uptake of targeted MSNP-PEG-MUC16 in comparison with untargeted MSNP-PEG in the OVCAR-3 cell line (Fig. 5A).

Furthermore, based on our results in SK-OV-3 cells, the untargeted MSNP-PEG/SUN showed higher internalization than targeted MSNP-PEG/SUN-MUC16 (Fig. 5B); this may be due to the steric hindrance by MUC16 aptamer that limits the association of NSs with the cell surface. Fig. 5C and 5D show the uptake data histogram in both cell lines.
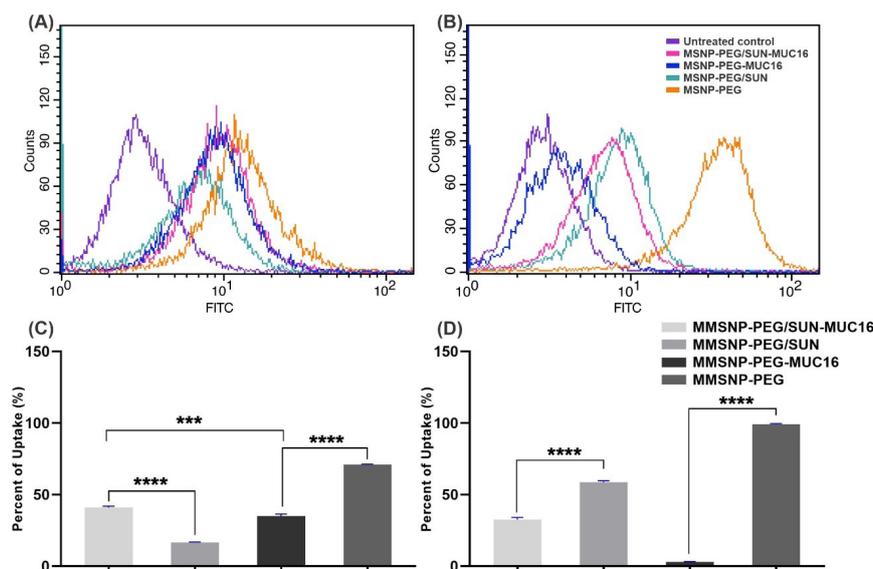
Cell cycle analysis

The cycle analysis was performed to determine the distribution of cell population in each stage. Fig. 6 displays the distribution in OVCAR-3 and SK-OV-3

cells in different phases. The untreated control cells showed a normal distribution. In OVCAR-3 cells treated with MSNP-PEG/SUN-MUC16, there was a significant decrease ($P \leq 0.0001$) in the cell population in the G0/G1 and G2/M phases and a significant increase in Sub G1 phase contributing to the successful growth inhibition. These results confirmed the efficiency of the aptamer-armed nanoparticles and their anti-proliferative ability in mucin-16 positive cells.[30] In SK-OV-3 cell line which is known to be mucin-16 negative, the cells exposed to MSNP-PEG/SUN for 24 hours also resulted in a significant decrease ($P \leq 0.0001$) in the cell population at G0/G1 and G2/M phases contributing to the successful growth inhibition and a rise in Sub G1 phase population.[31,32] Fig. 6I and 6J represent the histogram of cell cycle analysis in OVCAR-3 and SK-OV-3 cells, respectively.

DAPI staining

The morphological changes of the nucleus in both cell lines were studied using DAPI staining. As pictured in Fig. 7 the apoptotic cells had fragmented and condensed chromatin which was observed more in MSNP-PEG/SUN-MUC16 treated OVCAR-3 cells than the MSNP-

Fig. 5. The flow cytometry analysis of the uptake of MSNP-PEG/SUN-MUC16, MSNP-PEG/SUN, MSNP-PEG-MUC16, MSNP-PEG by OVCAR-3 (A), and SK-OV-3 (B) cells. Panels (C) and (D) respectively represent the quantification of internalized NSs by OVCAR-3 and SK-OV-3 cells. Data are shown as mean ± SD. The asterisks represent following level of significance; not significant (ns.) $P \geq 0.05$, $*P \leq 0.05$, $**P \leq 0.01$, $***P \leq 0.001$, $****P \leq 0.0001$.

PEG/SUN treated ones. However, in the SK-OV-3 cells, more disintegrated parts were detected upon treatment with MSNP-PEG/SUN.
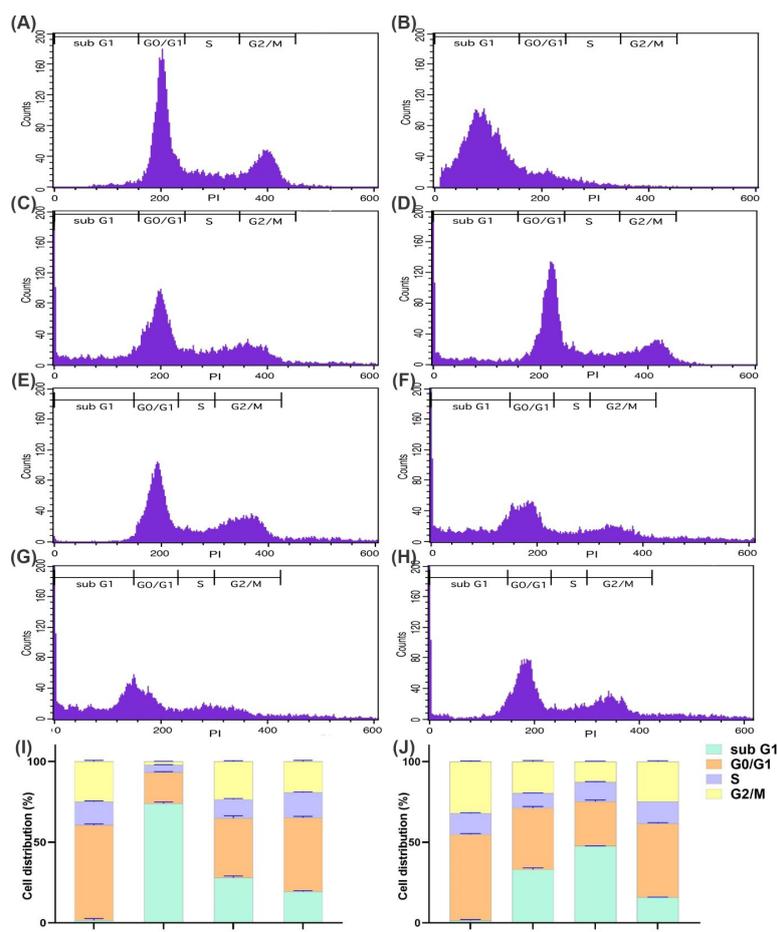
Discussion

As emerging DDSs, MSNPs has become one of the most widely investigated nanostructures, they have shown promising performances in preclinical studies.[15] They are shown to cut down the undesired adverse effects of antineoplastic agents.[13] SUN malate is a RTK inhibitor that has shown promising results in recurrent ovarian cancer, while undesired side effects have restrained its effectiveness.[33] Thus, the development of a targeted system for the delivery of SUN is an absolute requirement; this study aimed to design SUN-loaded MSNPs armed with MUC16 aptamer as a targeting ligand.

According to the schematic representation of Fig. 1, the preparation procedure initiated with the fabrication of MSNPs by the sol-gel method and continued by conjugating PEG_{600}-2NHS, SUN loading, and arming modified MUC16 aptamers. The PEGylation process can reduce nanoparticle removal by the reticuloendothelial system (RES) in macrophages and increase blood circulation and spread in tumor cells.[33-35] Various studies have shown that MSNPs accumulate in the lung, spleen, and liver, but conversely, when PEGylated, they spend more time in blood circulation.[36]

PEGylation neutralized the positive charge of amine-functionalized MSNPs and converted them into negatively-charged particles that were less harmful to cells.[37] Based on the TEM and SEM imaging (Fig. 2A and 2B), our nanoparticles had a uniform, spherical shape with a smooth surface, similar to the MSNPs synthesized by Lin et al.[38] According to Fig. 2C and 2D, the average size

of MSNPs and MSNP-PEG was about 56.1 and 103 nm, sequentially which are in the optimal size range for passive targeting of the TME by the EPR effect (approximately up to 300 nm in diameter).[39] The size of our synthesized MSNPs is comparable to previously reported results of the PEGylated drug-loaded MSNPs by Lin et al. and Kuang et al.[38,40]

The characterization of the nanoparticles is a key step to ensure that all functionalization/modification steps have been achieved. The accuracy of the developed method has been previously confirmed comprehensively by various assays such as HNMR spectroscopy,[41] which showed characteristic peaks corresponding to the designated structural groups. In this study we performed FTIR analysis to further confirm the synthesis and surface modification of NSs with essential characteristic bands related to MSNP, PEG_{600}-2NHS, MSNP-PEG, and MSNP-PEG/SUN (Fig. 3A).[27,42] To evaluate the porosity of the prepared MSNPs, N_2 ADS/DES was carried out. The N_2 ADS/DES isotherms plot and the ADS/DES trend showed a type-IV isotherm pattern according to IUPAC nomenclature. Upon using the BET analysis, the surface area of 148.08 m^2g^{-1} was calculated in the intermediate pressure range of $P/P0 = 0.01$-0.45 illustrated in Fig. 3B and 3C. As presented in Table 1, the BJH calculations revealed the mesoporous structure of MSNPs by calculating an average pore diameter of 2.488 nm in the range of 2-50 nm.[29,43] The MSNPs synthesized by Nandiyanto et al also exhibited similar N_2 ADS/DES isotherms to our targeted nanoparticles.[29] Further, the BJH calculations by Huang et al, who employed a similar method for MSNP synthesis, revealed a similar pore diameter.[43] The conjugation of the MUC16 aptamer to the surface of MSNP-PEG was confirmed by gel electrophoresis analysis (Fig. 3D). In

Fig. 5. The flow cytometry analysis of the uptake of MSNP-PEG/SUN-MUC16, MSNP-PEG/SUN, MSNP-PEG-MUC16, MSNP-PEG by OVCAR-3 (A), and SK-OV-3 (B) cells. Panels (C) and (D) respectively represent the quantification of internalized NSs by OVCAR-3 and SK-OV-3 cells. Data are shown as mean ± SD. The asterisks represent following level of significance; not significant (ns.) $P \geq 0.05$, $*P \leq 0.05$, $**P \leq 0.01$, $***P \leq 0.001$, $****P \leq 0.0001$.
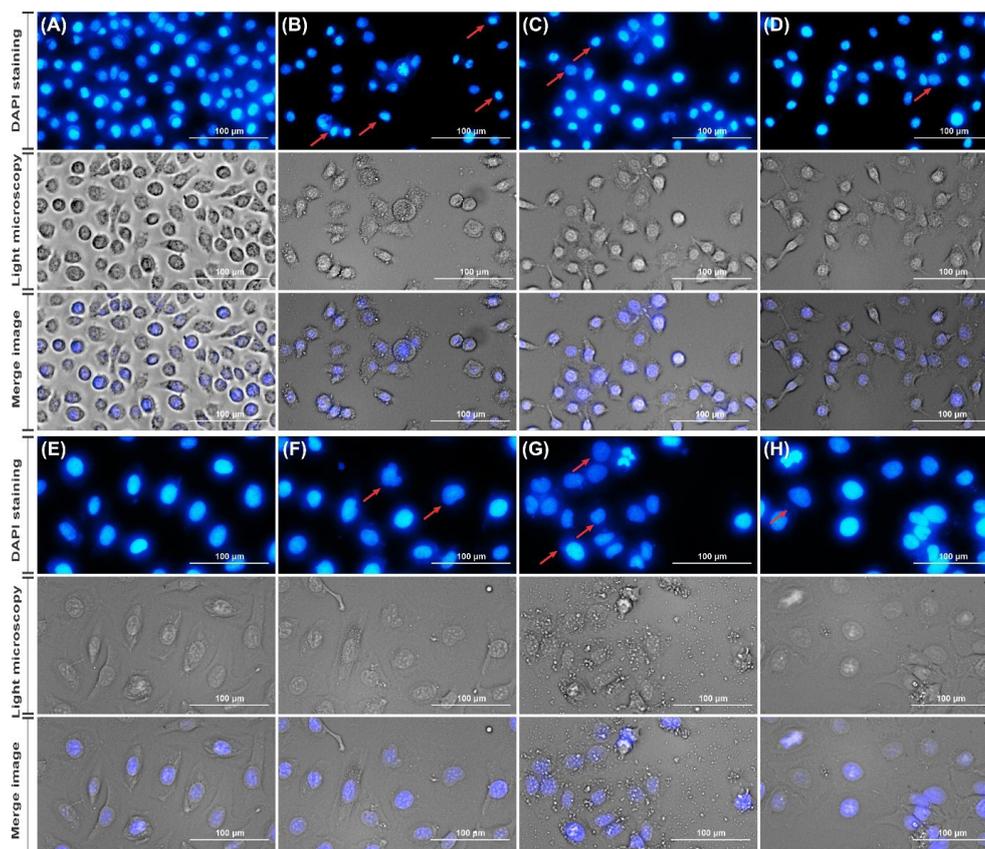
research by Li et al, for confirmation the conjugation of mesoporous strontium hydroxyapatite nano vehicle with AS1411 aptamer, agarose gel electrophoresis was carried out with a similar result.[44]

The XRD spectrum showed a sharp peak at $2\theta = 9$ and a broad peak at 20-27, that revealed a hexagonal amorphous structure (Fig. 3E).[45] In a research by Mu et al, the small nanocrystalline SiO_2/Al_2O_3 showed a peak at about 9 related to the silica.[46] The MSNPs synthesized by Vacca et al revealed a similar but sharp peak at 27 derived from TEOS.[47] Moreover, a research by Xue et al showed continuous broad spectrums at 22-37 for amorphous silica particles.[48]

SUN release from MSNPs in phosphate buffer at the physiological pH (i.e. 7.4) reached the maximum level of $14.16 \pm 0.94\%$ after 48 hours. However, in acidic environments (i.e. 6.4 and 5.4) at 37°C (Fig. 3F), the drug release increased significantly (i.e. $42.42 \pm 0.81\%$, and $59.69 \pm 0.91\%$, respectively), which implies that the prepared formulations show somewhat pH-responsive drug release. According to the pKa and structure of SUN (pKa = 9.8), the corresponding increase in drug release can be explicated by enhancing solubility of SUN due to the

protonated amine groups of SUN at the lower pH values.[49] The data showed a slight release of MSNP-PEG/SUN at the physiological environment while reaching TME, reducing the undesired side effects upon intravenous injection before reaching the desired target site.[50] Li et al reported a pH-dependent release of the co-condensation method synthesized MSNPs.[51]

According to the MTT results presented in Fig. 4, the cell viability of MSNP-PEG/SUN-MUC16 treated OVCAR-3 cells was remarkably lower than the untargeted MSNP-PEG/SUN ($P<0.001$), confirming the efficiency of the MUC16 aptamer as a targeting agent. Expectedly, the toxicity of MSNP-PEG/SUN in SK-OV-3 cells was higher than MSNP-PEG/SUN-MUC16. It should be noted that neither MSNP-PEG-MUC16 nor MSNP-PEG caused noticeable toxicity on the cell lines which demonstrated our carrier is cytocompatible in the range of the concentration tested. Xie et al. also reported higher toxicity of EpCAM aptamer functionalized MSNPs in EpCAM expressing colon cancer cells as compared with EpCAM non-expressing cells.[52] According to Xiong et al biotin-F87-polylactic acid and biotin-P85-polylactic acid armed with CA125 depicted more efficiency in a positive

Fig. 7. The morphological analysis and DAPI staining in OVCAR-3 cells treated with normal media as control (A), MSNP-PEG/SUN-MUC16 (B) MSNP-PEG/SUN (C) and SUN (D); also in SK-OV-3 cells treated with normal media as control (E), MSNP-PEG/SUN-MUC16 (F) MSNP-PEG/SUN (G) and SUN (H).

cell line (OVCAR-3) compared to negative cells (SK-OV-3).[53]

As previously stated, it has been determined that mucin 16 is overexpressed on the surface of the OVCAR-3 cells and there is no detectable expression of it on SK-OV-3 cells.[23] According to Fig. 5, there was an escalated uptake of the MSNP-PEG armed with MUC16 aptamer compared with MSNP-PEG/SUN in the uptake study of OVCAR-3 cells. In SK-OV-3 cells, there was a decrease in the uptake level of aptamer conjugated nanoparticles. It can be presumed that the interaction of the MUC16 aptamer with its specific cell membrane receptor causes the accumulation inside the targeted cells. However, because of interaction of negatively charged MUC16 aptamer with the cell surface as well as the spatial hindrance which further limits the access to the surface of cells uptake in negative cell lines.[54,55] Hence, due to a low spatial hindrance of untargeted MSNP-PEG, the topmost internalization is achieved upon treatment (70% in OVCAR-3 cells and 99% in SK-OV-3 cells).

The uptake of MSNP-PEG/SUN-MUC16 and MSNP-PEG/SUN in OVCAR-3 cells (40.92% and 16.54%, respectively) showed that conjugation with MUC16 aptamer has led to the selective uptake of the MSNPs in MUC16 expressing cell lines. The mucin 1 capped MSNPs synthesized by Pascual et al exhibited fairly similar uptake results as our targeted nanoparticles with MUC16 aptamer.[56]

Cell cycle analysis was performed upon treatment to determine the cell distribution in various cell cycle stages. As indicated in Fig. 6, MSNP-PEG/SUN-MUC16 induced the cell cycle arrest in the sub-G1 phase, ultimately leading to the population increase in sub-G1 and reducing the population of cells in the G2/M phase means the growth inhibition and apoptosis induction in MUC16 expressing cells. The results confirmed the anti-proliferative activity of aptamer-armed NSs in the positive cell line, consistent with Reinartz et al.'s results.[57] Additionally, the results of cell cycle analysis on MUC16 negative cells showed a high sub-G1 population in MSNP-PEG/SUN exposed cells.

Likewise, the DAPI staining assay illustrated the morphological changes in the nucleus and DNA-strand damage. According to Fig. 7, the MSNP-PEG/SUN-MUC16 treated OVCAR-3 cells showed the most detectable chromatin condensation. Further, it was more noticeable in MSNP-PEG/SUN treated SK-OV-3 cells. According to Wen et al, the bladder transitional carcinoma cells treated with SUN showed similar DNA damage to our targeted nanoparticles with MUC16 aptamer.[58]

Conclusion
Collectively in the current investigation, SUN-loaded

MSNP-PEG was decorated with MUC16 aptamer as a targeting ligand toward CA125 expressing ovarian cancer cells. Morphologically, MSNP-PEG was spherical and uniform with an average size of 103 nm. MSNP-PEG/SUN displayed a remarkably higher release in pH 5.4 (mimicking the TME), which may be considered a targeted drug release system if administered in-vivo. Further, conjugation of MUC16 led to higher internalization and toxicity in MUC16 positive OVCAR-3 cells compared to the MUC16 negative SK-OV-3 cells. These results indicated that targeted delivery of SUN via engineered MSNPs functionalized with MUC16 aptamer was effective at the cellular level. Whilst this study could only be considered as a proof-of-concept for the fabrication of a potentially effective DDS, it is crucial to perform *in vivo* studies in ovarian cancer models, with MUC16 positive and negative characteristics, to confirm the efficacy and safety of the engineered NSs. In addition, loading another therapeutic agent that might have a synergic effect with SUN, could enhance the efficiency of the treatment. In conclusion, MSNP-PEG/SUN-MUC16 is envisioned to be a suitable multifunctional nanomedicine for the therapeutic application against MUC16 overexpressing cancers.

Research Highlights

What is the current knowledge?
√ MSNPs are a suitable candidate for drug delivery and targeting.
√ SUN has demonstrated a promising therapeutic strategy to combat ovarian cancer.
√ CA125 is a valuable biomarker for the diagnosis of ovarian cancer.
√ Mucin 16 aptamer can target CA125 efficiently on the cancer cells.

What is new here?
√ To the best of our knowledge, it is the first investigation on the application of mesoporous silica NPs armed with Mucin-16 aptamer for the targeted delivery of SUN.
√ The successful characterization was confirmed using Fourier transform infrared, transmission electron microscopy, scanning electron microscope, dynamic light scattering, X-ray diffraction analysis, Barrett-Joyner-Halenda, and Brunauer-Emmett-Teller analysis, and various biological studies.
√ The in vitro biological evaluations demonstrated that the fabricated NS is a potentially suitable delivery system.
√ The presented data provide a proof of concept for the efficiency of our strategy, that is, the surface modification of MSNP through PEGylation and conjugation with MUC16 aptamer to combat CA125 expressing ovarian cancer cells.

References
1. Brodsky BS, Owens GM, Scotti DJ, Needham KA, Cool CL. Economic impact of increased utilization of multivariate assay testing to guide the treatment of ovarian cancer: Implications for payers. *Am Health Drug Benefits* **2017**; 10: 351-8. PMID: 29263770.
2. Siegel RL, Miller KD, Fuchs HE, Jemal A. Cancer Statistics, 2021. *CA Cancer J Clin* **2021**; 71: 7-33. https://doi.org/10.3322/caac.21654
3. Ayuob A, Jalilian AR, Yousef F, Davood B, Behrooz F, Ali K. Radiosynthesis and biodistribution studies of [^{62}Zn/^{62}Cu]-plerixafor complex as a novel in vivo PET generator for chemokine receptor imaging. *J Radioanal Nucl Chem* **2014**; 299: 1635-44. https://doi.org/10.1007/s10967-013-2822-2
4. Matulonis UA, Sood AK, Fallowfield L, Howitt BE, Sehouli J, Karlan BY. Ovarian cancer. *Nat Rev Dis Primers* **2016**; 2: 16061. https://doi.org/10.1038/nrdp.2016.61
5. Lheureux S, Braunstein M, Oza AM. Epithelial ovarian cancer: Evolution of management in the era of precision medicine. *CA Cancer J Clin* **2019**; 69: 280-304. https://doi.org/10.3322/caac.21559
6. Donnelly E, Chioato S, Taylor D. Chapter 20 - Anticancer Drug Registration and Regulation: Current Challenges and Possible Solutions. In: Neidle S, editor. *Cancer Drug Design and Discovery (Second Edition)*. San Diego: Academic Press; **2014**. p. 583-607.
7. Kurman RJ, Shih I-M. The Dualistic Model of Ovarian Carcinogenesis: Revisited, Revised, and Expanded. *Am J Pathol* **2016**; 186: 733-47. https://doi.org/10.1016/j.ajpath.2015.11.011
8. Biagi JJ, Oza AM, ChalChal HI, Grimshaw R, Ellard SL, Lee U, et al. A phase II study of sunitinib in patients with recurrent epithelial ovarian and primary peritoneal carcinoma: an NCIC Clinical Trials Group Study. *Ann Oncol* **2011**; 22: 335-40. https://doi.org/10.1093/annonc/mdq357
9. Baumann KH, du Bois A, Meier W, Rau J, Wimberger P, Sehouli J, *et al.* A phase II trial (AGO 2.11) in platinum-resistant ovarian cancer: a randomized multicenter trial with sunitinib (SU11248) to evaluate dosage, schedule, tolerability, toxicity and effectiveness of a multitargeted receptor tyrosine kinase inhibitor monotherapy. *Ann Oncol* **2012**; 23: 2265-71. https://doi.org/10.1093/annonc/

mds003

10. Saberian M, Hamzeiy H, Aghanejad A, Asgari D. Aptamer-based nanosensors: juglone as an attached-redox molecule for detection of small molecules. *BioImpacts* **2011**; 1: 31. https://doi.org/10.5681/bi.2011.005

11. Du Z, Lovly CM. Mechanisms of receptor tyrosine kinase activation in cancer. *Mol Cancer* **2018**; 17: 58. https://doi.org/10.1186/s12943-018-0782-4

12. Asgari D, Aghanejad A, Mojarrad JS. An improved convergent approach for synthesis of erlotinib, a tyrosine kinase inhibitor, via a ring closure reaction of phenyl benzamidine intermediate. *Bull Korean Chem Soc* **2011**; 32: 909-14. https://doi.org/10.5012/bkcs.2011.32.3.909

13. Manzano M, Vallet-Regí M. Mesoporous Silica Nanoparticles for Drug Delivery. *Adv Funct Mater* **2020**; 30: 1902634. https://doi.org/10.1002/adfm.201902634

14. Siminzar P, Omidi Y, Golchin A, Aghanejad A, Barar J. Targeted delivery of doxorubicin by magnetic mesoporous silica nanoparticles armed with mucin-1 aptamer. *J Drug Target* **2020**; 28: 92-101. https://doi.org/10.1080/1061186X.2019.1616745

15. Narayan R, Nayak UY, Raichur AM, Garg S. Mesoporous silica nanoparticles: A comprehensive review on synthesis and recent advances. *Pharmaceutics* **2018**; 10. https://doi.org/10.3390/pharmaceutics10030118

16. Hicke BJ, Stephens AW, Gould T, Chang Y-F, Lynott CK, Heil J, et al. Tumor Targeting by an Aptamer. *J Nucl Med* **2006**; 47: 668. PMID: 16595502.

17. Borran AA, Aghanejad A, Farajollahi A, Barar J, Omidi Y. Gold nanoparticles for radiosensitizing and imaging of cancer cells. *Radiat Phys Chem* **2018**; 152: 137-44. https://doi.org/10.1016/j.radphyschem.2018.08.010

18. Castillo RR, Colilla M, Vallet-Regí M. Advances in mesoporous silica-based nanocarriers for co-delivery and combination therapy against cancer. *Expert Opin Drug Deliv* **2017**; 14: 229-43. https://doi.org/10.1080/17425247.2016.1211637

19. Streppel MM, Vincent A, Mukherjee R, Campbell NR, Chen SH, Konstantopoulos K, et al. Mucin 16 (cancer antigen 125) expression in human tissues and cell lines and correlation with clinical outcome in adenocarcinomas of the pancreas, esophagus, stomach, and colon. *Hum Pathol* **2012**; 43: 1755-63. https://doi.org/10.1016/j.humpath.2012.01.005

20. Kanwal M, Ding XJ, Song X, Zhou GB, Cao Y. MUC16 overexpression induced by gene mutations promotes lung cancer cell growth and invasion. *Oncotarget* **2018**; 9: 12226-39. https://doi.org/10.18632/oncotarget.24203

21. Scoville DJ, Uhm TKB, Shallcross JA, Whelan RJ. Selection of DNA Aptamers for Ovarian Cancer Biomarker CA125 Using One-Pot SELEX and High-Throughput Sequencing. *J Nucleic Acids* **2017**; 2017. https://doi.org/10.1155/2017/9879135

22. Goodell CAR, Belisle JA, Gubbels JAA, Migneault M, Rancourt C, Connor J, et al. Characterization of the tumor marker muc16 (ca125) expressed by murine ovarian tumor cell lines and identification of a panel of cross-reactive monoclonal antibodies. *J Ovarian Res* **2009**; 2: 8. https://doi.org/10.1186/1757-2215-2-8

23. Giannakouros P, Comamala M, Matte I, Rancourt C, Piché A. MUC16 mucin (CA125) regulates the formation of multicellular aggregates by altering β-catenin signaling. *Am J Cancer Res* **2014**; 5: 219-30. PMID: 25628932; PMCID: PMC4300699.

24. Felder M, Kapur A, Gonzalez-Bosquet J, Horibata S, Heintz J, Albrecht R, *et al.* MUC16 (CA125): tumor biomarker to cancer therapy, a work in progress. *Mol Cancer* **2014**; 13: 129-. https://doi.org/10.1186/1476-4598-13-129

25. van Meerloo J, Kaspers GJ, Cloos J. Cell sensitivity assays: the MTT assay. *Methods Mol Biol* **2011**; 731: 237-45. https://doi.org/10.1007/978-1-61779-080-5_20

26. Mandelkow R, Gümbel D, Ahrend H, Kaul A, Zimmermann U, Burchardt M, *et al.* Detection and Quantification of Nuclear Morphology Changes in Apoptotic Cells by Fluorescence Microscopy and Subsequent Analysis of Visualized Fluorescent Signals. *Anticancer Res* **2017**; 37: 2239-44. https://doi.org/10.21873/anticanres.11560

27. Singh A, Shirolkar M, Limaye MV, Gokhale S, Khan-Malek C, Kulkarni SK. A magnetic nano-composite soft polymeric membrane. *Microsyst Technol* **2013**; 19: 409-18. https://doi.org/10.1007/s00542-012-1646-2

28. Joseph JJ, Sangeetha D, Gomathi T. Sunitinib loaded chitosan nanoparticles formulation and its evaluation. *Int J Biol Macromol* **2016**; 82: 952-8. https://doi.org/10.1016/j.ijbiomac.2015.10.079

29. Nandiyanto ABD, Kim S-G, Iskandar F, Okuyama K. Synthesis of spherical mesoporous silica nanoparticles with nanometersize controllable pores and outer diameters. *Microporous Mesoporous Mater* **2009**; 120: 447-53. https://doi.org/10.1016/j.micromeso.2008.12.019

30. He Q, Gao Y, Zhang L, Zhang Z, Gao F, Ji X, *et al.* A pH-responsive mesoporous silica nanoparticles-based multi-drug delivery system for overcoming multi-drug resistance. *Biomaterials* **2011**; 32: 7711-20. https://doi.org/10.1016/j.biomaterials.2011.06.066

31. Kumar RMR, Arlt MJ, Kuzmanov A, Born W, Fuchs B. Sunitinib malate (SU-11248) reduces tumour burden and lung metastasis in an intratibial human xenograft osteosarcoma mouse model. *Am J Cancer Res* **2015**; 5: 2156-68. PMID: 26328246; PMCID: PMC4548327.

32. Juengel E, Kim D, Makarević J, Reiter M, Tsaur I, Bartsch G, et *al.* Molecular analysis of sunitinib resistant renal cell carcinoma cells after sequential treatment with RAD001 (everolimus) or sorafenib. *J Cell Mol Med* **2015**; 19: 430-41. https://doi.org/10.1111/jcmm.12471

33. Macdonald JB, Macdonald B, Golitz LE, LoRusso P, Sekulic A. Cutaneous adverse effects of targeted therapies: Part I: Inhibitors of the cellular membrane. *J Am Acad Dermatol* **2015**; 72: 203-18. https://doi.org/10.1016/j.jaad.2014.07.032

34. Beltrán-Osuna ÁÁ, Perilla JE. Colloidal and spherical mesoporous silica particles: synthesis and new technologies for delivery applications. *J Solgel Sci Technol* **2016**; 77: 480-96. https://doi.org/10.1007/s10971-015-3874-2

35. Matsumura Y, Maeda H. A new concept for macromolecular therapeutics in cancer chemotherapy: mechanism of tumoritropic accumulation of proteins and the antitumor agent smancs. *Cancer Res* **1986**; 46: 6387-92.

36. Foroughi-Nia B, Barar J, Memar MY, Aghanejad A, Davaran S. Progresses in polymeric nanoparticles for delivery of tyrosine kinase inhibitors. *Life Sci* **2021**; 278: 119642. https://doi.org/10.1016/j.lfs.2021.119642

37. Verma A, Stellacci F. Effect of surface properties on nanoparticle-cell interactions. *Small* **2010**; 6: 12-21. https://doi.org/10.1002/smll.200901158

38. Lin J, Cai Q, Tang Y, Xu Y, Wang Q, Li T, *et al.* PEGylated Lipid bilayer coated mesoporous silica nanoparticles for co-delivery of paclitaxel and curcumin: Design, characterization and its cytotoxic effect. *Int J Pharm* **2018**; 536: 272-82. https://doi.org/10.1016/j.ijpharm.2017.10.043

39. Kobayashi H, Watanabe R, Choyke PL. Improving conventional enhanced permeability and retention (EPR) effects; what is the appropriate target? *Theranostics* **2013**; 4: 81-9. https://doi.org/10.7150/thno.7193

40. Kuang G, Zhang Q, He S, Liu Y. Curcumin-loaded PEGylated mesoporous silica nanoparticles for effective photodynamic therapy. *RSC Adv* **2020**; 10: 24624-30. https://doi.org/10.1039/D0RA04778C

41. Hashemzadeh N, Dolatkhah M, Aghanejad A, Barzegar-Jalali M, Omidi Y, Adibkia K, *et al.* Folate receptor-mediated delivery of 1-MDT-loaded mesoporous silica magnetic nanoparticles to target breast cancer cells. *Nanomedicine (Lond)* **2021**; 16: 2137-54. https://doi.org/10.2217/nnm-2021-0176

42. Aghanejad A, Babamiri H, Adibkia K, Barar J, Omidi Y. Mucin-1 aptamer-armed superparamagnetic iron oxide nanoparticles for targeted delivery of doxorubicin to breast cancer cells. *Bioimpacts* **2018**; 8: 117-27. https://doi.org/10.15171/bi.2018.14

43. Huang X, Young NP, Townley HE. Characterization and comparison of mesoporous silica particles for optimized drug

delivery. *Nanomater Nanotechnol* **2014**; 4: 4-2. https://doi.org/10.5772/58290

44. Li Z, Liu Z, Yin M, Yang X, Yuan Q, Ren J, *et al.* Aptamer-Capped Multifunctional Mesoporous Strontium Hydroxyapatite Nanovehicle for Cancer-Cell-Responsive Drug Delivery and Imaging. *Biomacromolecules* **2012**; 13: 4257-63. https://doi.org/10.1021/bm301563q

45. Sarawade PB, Kim J-K, Hilonga A, Kim HT. Recovery of high surface area mesoporous silica from waste hexafluorosilicic acid (H2SiF6) of fertilizer industry. *J Hazard Mater* **2010**; 173: 576-80. https://doi.org/10.1016/j.jhazmat.2009.08.125

46. Mu L, Feng W, Zhang H, Hu X, Cui Q. Synthesis and catalytic performance of a small crystal NaY zeolite with high SiO2/Al2O3 ratio. *RSC Adv* **2019**; 9: 20528-35. https://doi.org/10.1039/C9RA03324F

47. Vacca MA, Cara C, Mameli V, Sanna Angotzi M, Scorciapino MA, Cutrufello MG, *et al.* Hexafluorosilicic Acid (FSA): from Hazardous Waste to Precious Resource in Obtaining High Value-Added Mesostructured Silica. *ACS Sustain Chem Eng* **2020**; 8: 14286-300. https://doi.org/10.1021/acssuschemeng.0c03218

48. Xue S-H, Xie H, Ping H, Li Q-C, Su B-L, Fu Z-Y. Induced transformation of amorphous silica to cristobalite on bacterial surfaces. *RSC Adv* **2015**; 5: 71844-8. https://doi.org/10.1039/C5RA13619A

49. Karimi MH, Mahdavinia GR, Massoumi B. pH-controlled sunitinib anticancer release from magnetic chitosan nanoparticles crosslinked with κ-carrageenan. *Mater Sci Eng C Mater Biol Appl* **2018**; 91: 705-14. https://doi.org/10.1016/j.msec.2018.06.019

50. Vallet-Regí M, Colilla M, Izquierdo-Barba I, Manzano M. Mesoporous Silica Nanoparticles for Drug Delivery: Current Insights. *Molecules* **2017**; 23: 47. https://doi.org/10.3390/molecules23010047

51. Li L-L, Yin Q, Cheng J, Lu Y. Polyvalent Mesoporous Silica Nanoparticle-Aptamer Bioconjugates Target Breast Cancer Cells.

Adv Healthc Mater **2012**; 1: 567-72. https://doi.org/10.1002/adhm.201200116

52. Xie X, Li F, Zhang H, Lu Y, Lian S, Lin H, *et al.* EpCAM aptamer-functionalized mesoporous silica nanoparticles for efficient colon cancer cell-targeted drug delivery. *Eur J Pharm Sci* **2016**; 83: 28-35. https://doi.org/10.1016/j.ejps.2015.12.014

53. Xiong XY, Gong YC, Li ZL, Li YP, Guo L. Active targeting behaviors of biotinylated pluronic/poly(lactic acid) nanoparticles in vitro through three-step biotin-avidin interaction. *J Biomater Sci Polym Ed* **2011**; 22: 1607-19. https://doi.org/10.1163/092050610x519444

54. Ekkapongpisit M, Giovia A, Follo C, Caputo G, Isidoro C. Biocompatibility, endocytosis, and intracellular trafficking of mesoporous silica and polystyrene nanoparticles in ovarian cancer cells: effects of size and surface charge groups. *Int J Nanomedicine* **2012**; 7: 4147. https://doi.org/10.2147/IJN.S33803

55. Shuvaev VV, Khoshnejad M, Pulsipher KW, Kiseleva RY, Arguiri E, Cheung-Lau JC, *et al.* Spatially controlled assembly of affinity ligand and enzyme cargo enables targeting ferritin nanocarriers to caveolae. *Biomaterials* **2018**; 185: 348-59. https://doi.org/ 10.1016/j.biomaterials.2018.09.015

56. Pascual L, Cerqueira-Coutinho C, García-Fernández A, de Luis B, Bernardes ES, Albernaz MS, *et al.* MUC1 aptamer-capped mesoporous silica nanoparticles for controlled drug delivery and radio-imaging applications. *Nanomedicine* **2017**; 13: 2495-505. https://doi.org/ 10.1016/j.nano.2017.08.006

57. Reinartz S, Failer S, Schuell T, Wagner U. CA125 (MUC16) gene silencing suppresses growth properties of ovarian and breast cancer cells. *Eur J Cancer* **2012**; 48: 1558-69. https://doi.org/10.1016/j.ejca.2011.07.004

58. Wen J, Li H-Z, Ji Z-G, Jin J. Human urothelial carcinoma cell response to Sunitinib malate therapy in vitro. *Cancer Cell Int* **2015**; 15: 26. https://doi.org/10.1186/s12935-015-0179-z